Preparation of pH-Responsive Vesicular Deferasirox: Evidence from In Silico, In Vitro, and In Vivo Evaluations

Mahmood Barani, Saman Sargazi, Mohammad Reza Hajinezhad, Abbas Rahdar, Fakhara Sabir, Abbas Pardakhty, Farshid Zargari, Md Khalid Anwer, M. Ali Aboudzadeh

ACS OMEGA

http://pubs.acs.org/journal/acsodf

Article

Preparation of pH-Responsive Vesicular Deferasirox: Evidence from *In Silico*, *In Vitro*, and *In Vivo* Evaluations

Mahmood Barani, Saman Sargazi, Mohammad Reza Hajinezhad,* Abbas Rahdar,* Fakhara Sabir, Abbas Pardakhty, Farshid Zargari, Md. Khalid Anwer,* and M. Ali Aboudzadeh*

Cite This: *ACS Omega* 2021, 6, 24218−24232

Read Online

ACCESS | Metrics & More | Article Recommendations

ABSTRACT: pH-sensitive nanocarriers can effectively deliver anticancer drugs to tumors and reduce the adverse effects of conventional chemotherapy. In this light, we prepared a novel pH-responsive deferasirox (DFX)-loaded vesicle and comprehensively performed *in silico*, *in vitro*, and *in vivo* studies to examine the properties of the newly synthesized formulation. Physiochemical assessment of the developed formulations showed that they have an average size (107 ± 2 nm), negative zeta potential (−29.1 ± 1.5 mV), high encapsulation efficiency (84.2 ± 2.6%), and a pH-responsive release. Using the molecular dynamics simulation, the structural and dynamic properties of ergosterol-containing niosomes (ST60/Ergo) in the presence of DFX molecules were analyzed and showed a good interaction between DFX and vesicle components. Cytotoxic assessment showed that niosomal DFX exhibited a greater cytotoxic effect than free DFX in both human cancer cells (MCF-breast cancer and Hela cervical cancer) and induced evident morphological features of apoptotic cell death. No marked difference between the ability of free and niosomal DFX was found in activating caspase-3 in Hela cells. Eight weeks of intraperitoneal administrations of free DFX at three doses caused a significant increase in serum biochemical parameters and liver lipid peroxidation. Treatment with 5 mg/kg dose of niosomal DFX caused a significant increase in serum creatinine ($P < 0.05$); however, other parameters remained unchanged. On the other hand, administration of niosomal DFX at the highest dose (10 mg/kg) significantly increased serum creatinine ($P < 0.05$), BUN, and serum liver enzymes compared to the control rats ($P < 0.001$). Based on the results, the application of pH-responsive DFX-loaded niosomes, as a novel drug delivery platform, may yield promising results in cancer treatment.

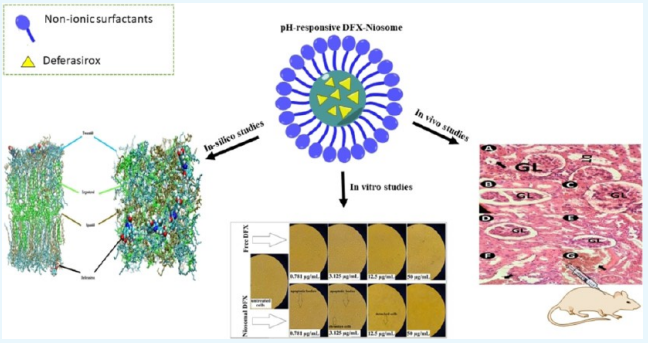

1. INTRODUCTION

Deferasirox (DFX) is an iron chelator and was approved for the treatment of transfusional iron. It is a N-substituted bis-hydroxyphenyl-triazole, tridentate chelator, and such two molecules are combined to form a stable complex with a single iron ion. The active molecule is highly lipophilic and 99% albumin bound. DFX has a greater and specific affinity for iron than other ions such as copper and zinc.[1] DFX is well tolerated in both children and adults. The adverse effects observed during core clinical trials include gastrointestinal adverse reactions (e.g., vomiting, nausea, constipation, and diarrhea) and many skin problems.[2,3] Several clinical studies suggested that its serum concentration is directly proportional to the given dose. The *in vivo* animal studies showed that DFX can be absorbed quickly from the gut and can mobilize iron from different organ systems, including cardiomyocytes and hepatocytes. The DFX treatment in humans was achieved via a dose rise study in patients through transfusional iron overload and b-thalassemia.[4] DFX is also an antineoplastic agent, and over the past few years, the potential for DFX to act as a cytotoxic agent has been studied.[5] The human data comprises only a small series and variable case studies. Anticancer studies have been shown to decrease cellular viability, inhibit DNA replication, and induce DNA fragmentation in human hepatoma cell lines and normal human primary cultures.[6,7]

In contrast to the other iron chelators, DFX creates cell cycle blockade during the S-phase rather than the G1 phase. Moreover, a greater amount of DFX is needed to induce cytotoxicity in primary hepatocyte cultures than hepatoma cells. The DFX exposure can also cause a marked reduction of ornithine decarboxylase (ODC) mRNA levels, resulting in

Received: July 18, 2021
Published: September 13, 2021

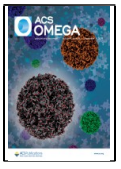

reduced cell viability and DNA replication. Oral DFX significantly reduces the xenograft size on mouse health, biochemical parameters, and hemoglobin levels. DFX could enhance the expression of the metastasis suppressor protein, N-myc downstream regulated gene-1 (NDRG1), and unregulated the cyclin-dependent kinase inhibitor p21CIP1/WAF1.[8,9] Concerning the study's findings on myeloid leukemia cells, the drug could also increase the expression of apoptosis markers, including caspase-3 (a serine protease that induces apoptosis). DFX has demonstrated anticancer applications against various cancer cell lines, indicating that cancer cells require a large amount of iron compared to the normal cells to intercede their quick DNA proliferation and replication. DFX is relatively lipophilic in nature and belongs to biopharmaceutics class II (BCS II) and is characterized by its low solubility (0.038 mg/mL at 37 °C), low dissolution rate, and enhanced intestinal permeability. The dissolution of active pharmaceutical ingredients is the rate-determining step for absorbing BCS class II compounds such as DFX.[10]

To enhance the aqueous solubility of DFX, it is crucial to synergize its oral bioavailability. There is a need to fulfill the requirement of a high dose of DFX to show its therapeutic effects. Therefore, it is necessary to reformulate the DFX-encapsulated formulation with greater solubility and bioavailability.

Nanotechnology has many remarkable applications in different industries.[11−15] The nanodrug carrier systems deliver therapeutic agents because of their ability and enhanced efficiency to encapsulate both hydrophilic and hydrophobic drug molecules and can also be used in bioimaging applications.[16,17] Today, nanotechnology-based diagnostic assays and therapeutic procedures fall within the scope of a broader field known as nanomedicine, which is heavily dependent on developing novel nanocarriers.[18−21] In addition to diagnosis and monitoring, nanotechnology has also contributed to developing novel therapies for a variety of diseases and cancers.[22−26] These nanocarriers protect the encapsulated drugs from physiological degradation, which assist with solubility, and ensure the sustained/controlled release of the drug from the carrier with a precise delivery rate and dose regimen to increase its bioavailability level.[27] Among novel noncarriers, niosome gained a lot of attention in recent years.

Niosomes are vesicular systems consisted of non-ionic surfactants and cholesterol, are biocompatible and biodegradable, and can be produced in a low-cost process.[28] Several niosomal formulations have recently shown promising results as a novel drug delivery system to combat cancer. Marzban et al. prepared nano-niosome particles loaded with DFX for the patients having primary or secondary iron overload deficiency. The unique feature of niosome enables sustained release of the drug for long periods. The biocompatibility studies of DFX-encapsulated niosomes reduce the toxicity of DFX significantly. The results demonstrated that a greater concentration of DFX was found at the targeting site from niosomes than the free drug.[29] Another study from the same research group developed DFX-loaded niosomes for the treatment of iron overload disorders. The results showed greater efficiency of DFX when encapsulated into niosomes in systemic circulation for iron overload disorder.[30] Also, modification on niosome is another approach to enhance their abilities. In niosome preparation, a helper lipid such as cholesterol was used. In our previous study, we observed that using ergosterol instead of cholesterol can improve formulation efficiency.

Ergosterol (ergosta-5,7, 22-trien-3β-ol) is a sterol found in the cell membranes of fungi and protozoa with the same functions as cholesterol in animal cells. Ergosterol and cholesterol have a similar morphology, including the molecule's length and common features, including a planar cyclopentane-phenantrene ring, a 3β-OH group, and a hydrophobic side chain linked to C17. The morphological differences of ergosterol compared to cholesterol include two additional double bonds, one in the rigid ring at position C7 and the other in its tail at C22, and a methyl group on the side chain at C24.[31,32] The presence of the double bond in the ring has been proposed to increase the interactions between phospholipid acyl chains and ergosterol due to the increased van der Waals forces, causing the planarity of the ring and probably the sustained release of the drug. Several ways have been used to increase the stability, encapsulation efficiency, and pharmacokinetic behavior of vesicular systems.[31,33,34]

The development of formulation with pH-sensitive materials (such as CHEMS) may regulate, modulate, and help to evaluate the aggregation, distribution, and metabolism *in vivo*. For example, Eudragit-coated liposomes were developed by Caddeo et al.[35] The proposed formulation served two purposes: protecting the vesicles from acidic degradation and allowing the release of the payload in the region of the intestinal tract with near-neutral pH (i.e., the large intestine or colon). Cholesteryl hemisuccinate (CHEMS) is an acidic cholesterol ester that self-assembles in alkaline and neutral aqueous media into bilayers and is broadly applied in the surfactant mixture to produce pH-sensitive vesicles.[36,37] Baranei et al. evaluated the anticancer effect of green tea extract (GTE)-loaded pH-responsive niosome coated with PEG against different cell lines. The pH-responsive formulation provided a pH-sensitive sustained-release followed Higuchi release kinetics.[38]

In this research, we have developed a pH-responsive DFX-loaded vesicle modified with ergosterol and CHEMS for effective cancer therapy applications. In our previous studies, we observed that using ergosterol instead of cholesterol can improve the efficiency of niosome formulation[31] and also observed that DFX-loaded nanomicelles exhibited greater cytotoxic effects than free DFX in HepG2 liver cancer cells and lower toxicity in normal HUVEC cells.[1] The prepared formulation was evaluated in terms of physicochemical properties, *in vitro* cytotoxicity, and *in vivo* anticancer potential. Also, molecular dynamics (MD) simulations were applied for better understanding of prepared formulation and its interaction mechanisms. As far as we know, there is no similar study for effective pH-responsive delivery of DFX and also evaluate all aspects of *in silico*, *in vitro*, and *in vivo* experiments.

2. RESULTS

2.1. Simulation. *2.1.1. Bilayer Structure.* Dynamic simulation, experimental design, and other *in silico* programs are useful tools to avoid unnecessary experiments.[39−42] These modeling approaches use computer science to model the time-varying behavior of a dynamical system.[43−46] One of the main properties related to membrane bilayer is area per lipid (APL), by which one can evaluate the phase transition of the lipid bilayer and the validation of the force field. However, we calculated the APL by using the *xy*-surface area of the simulation box divided by the number of Span 60, Tween 60,

https://doi.org/10.1021/acsomega.1c03816
ACS Omega 2021, 6, 24218−24232

Table 1. Comparison of the Structural Properties of Span 60, Tween 60, and Ergosterol Bilayers in 35:35:30% mol at the Beginning and End of MD Simulation

lipid	Span 60		Tween 60		ergosterol	
time	0 ns	40 ns	0 ns	40 ns	0 ns	40 ns
APL (Å^2)	24.69 ± 0.1	22.26 ± 0.1	25.31 ± 0.1	22.82 ± 0.1	28.92 ± 0.1	26.08 ± 0.1
thickness (nm)	5.78 ± 0.001	5.92 ± 0.001	6.03 ± 0.001	6.95 ± 0.001	2.75 ± 0.001	2.85 ± 0.001

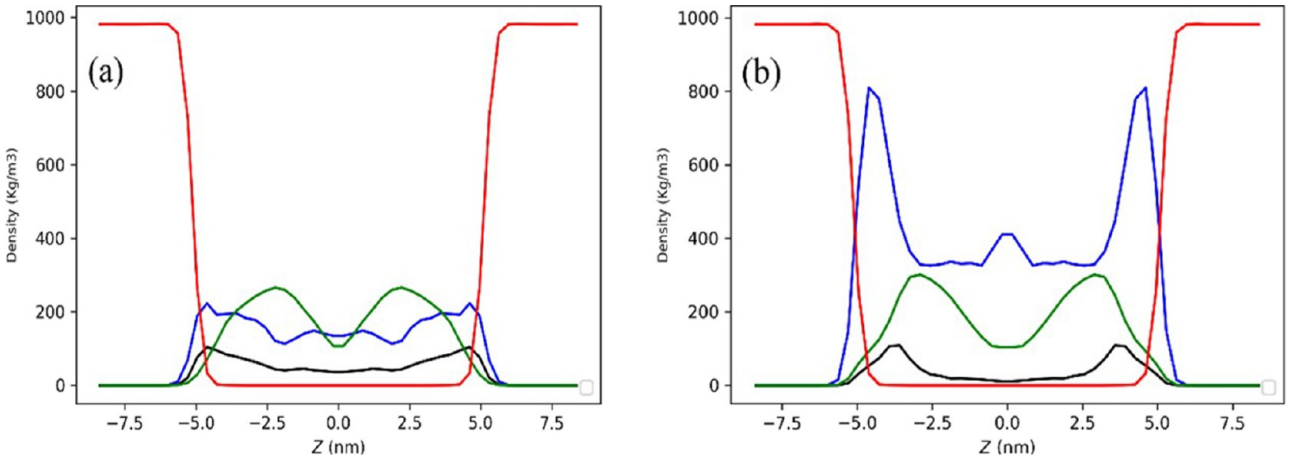

Figure 1. Mass density distributions for the headgroup (blue), ester group (black), acyl group (green), and water (red) of (a) Span 60 and (b) Tween 60 as a function of *z*-direction normalized to the bilayer plane.

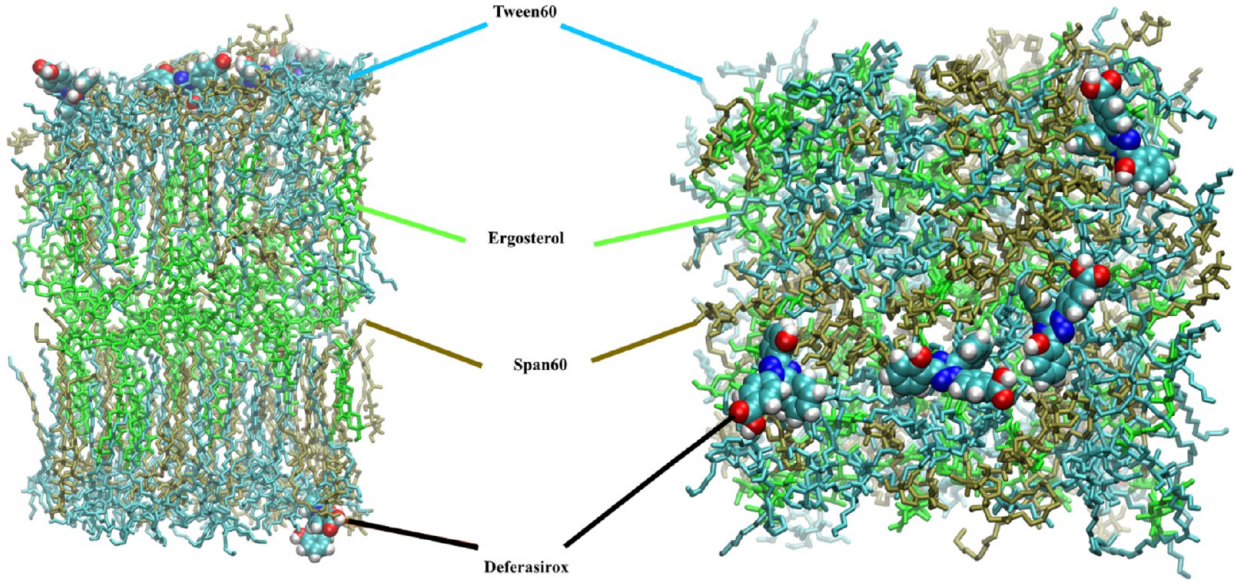

Figure 2. Molecular structure of DFX at the edge of lipid bilayer as facial (right) and lateral representation (left).

and ergosterol in the leaflet. Table 1 compares the structural properties, APL, and bilayer thickness of the niosome bilayer component used in this work at the beginning and at the end of simulation time. Span 60 has the average APL of 24.69 ± 0.1 Å^2 at the beginning of MD simulation, while this value was diminished to 22.26 ± 0.1 Å^2 at the end, which has great consistency with the experimental value (22 Å^2).[47] Insertion of Tween 60 and ergosterol to the Span 60 bilayer, which is closely packed with high-order orientation, does not expand the bilayer. Tween 60 and ergosterol possessed an average APL of 22.82 ± 0.1 and 26.08 ± 0.1 Å^2 after 40 ns MD simulation.

The bilayer thickness is another structural property of the bilayer system defined as the headgroup mass center of every bilayer component, that is, Span 60, Tween 60, and ergosterol. The calculated thicknesses at the beginning and the end of simulation for each component are represented in Table 1. It was seen that the bilayer thicknesses for Span 60, Tween 60, and ergosterol are 5.92 ± 0.001, 6.95 ± 0.001, and 2.85 ± 0.001 at the end of the simulation, respectively. The GridMAT-MD script[48] was utilized to calculate the APL and thickness of each lipid in the niosome bilayer.

2.1.2. Mass Density Profile. The mass density of molecules and some parts of the molecule, including the headgroup, the ester group, and the acyl group of Span 60, Tween 60, and water, are depicted in Figure 1. The distributions of mass density along the *z*-axis were calculated and displayed in a symmetric pattern, which provides the evidence of a well-equilibrated bilayer system.

https://doi.org/10.1021/acsomega.1c03816
ACS Omega 2021, 6, 24218−24232

Table 2. Average and Detailed Hydrogen Bond Analysis of DFX with Span 60, Tween 60, and Ergosterol in This Study

	hydrogen bonds		
	DFX-Span 60	DFX-Tween 60	DFX-ergosterol
average hydrogen number	1.23	1.36	0.03

	hydrogen bonds					
	DFX-Span 60		DFX-Tween 60		DFX-ergosterol	
	donor−acceptor	occupancy	donor−acceptor	occupancy	donor−acceptor	occupancy
detailed hydrogen bonds	[a]SPN@O28-DFX@O4	9.22	DFX@O3-TWN@O10	13.60	ERG@O1-DFX@O2	0.87
	SPN@O29-DFX@O1	8.77	DFX@O1-TWN@O10	12.40	ERG@O1-DFX@N6	0.80
	SPN@O29-DFX@O4	8.30	TWN@O8-DFX@O1	10.40	ERG@O2-DFX@O1	0.40
	SPN@O28-DFX@O3	7.23	TWN@O6-DFX@O1	10.10	ERG@O3-DFX@O1	0.37

[a]SPN: Span 60, TWN: Tween 60, ERG: ergosterol, and DFX: deferasirox.

Emersion of two wide peaks for the headgroup density of Span 60 overlapping with the water density alongside indicates that the Span 60 headgroup intends to reside at the water interface. This is much more apparent in the headgroup density of Tween 60 as two sharp narrow peaks emerged in the density profile of this species during the course of simulation. It is apparent from Figure 2 that in this type of bilayer, the headgroup densities of both Span 60 and Tween 60 do not tend to be zero at the center of the bilayer ($z = 0$). This can be attributed to the presence of ergosterol which can make some strong interactions with ester or hydroxyl groups of Span 60 and Tween 60 headgroups. According to Figure 2, the broadening of headgroup density peak is due to a trade-off between the tendency of forming H-bonds between the hydroxyl groups of Span 60/Tween 60 headgroups and ergosterol in one side and at the other side penetrating to the edge of water bulk phase for hydrogen bonding. It seems that this phenomenon can affect much more the Span 60 headgroup rather than the Tween 60 headgroup.

2.1.3. Hydrogen Bonding between the Membrane and DFX. In order to determine the stability of hydrogen bonds between three components of niosome bilayer (Span 60, Tween 60, and ergosterol) with DFX as a loading drug, MD analysis of the drug−bilayer complex stability was performed for a trajectory period of 40 ns. The hydrogen bond profiles between DFX and the lipids were calculated using the H-bond utility of Gromacs 2020.1. The threshold for H-bond forming was 3.5 Å with an angle of 30°. Figure 2 illustrates the average position of DFX on one side of the bilayer during the 40 ns MD simulation. It is evident from Figure 2 that in most periods of simulation time, the drugs are close to the edge of the bilayer, where they participated in strong interactions with lipids. More details for analysis of hydrogen bonds between DFX and Span 60, Tween 60, and ergosterol are shown in Table 2.

It is apparent from Table 2 that the interaction of DFX with ergosterol (the average hydrogen bond of ∼0.03) is much lower than the other components due to the further distance between these two species. Ergosterol intends to create a hydrogen bond through its headgroup with Span 60 and Tween 60.[49] Table 2 displays that the main interactions of DFX with the bilayer are through making strong hydrogen bonds with the Tween 60 headgroup. The related occupancy numbers to the lifetime of the hydrogen bond between O10, O8, and O1 atoms of Tween 60 with O3 and O1 atoms of DFX provide evidence for this assertion (Figure 12a). Likewise, although the hydrogen bonds are less strong than Tween 60, still noticeable ones took place between the DFX and Span 60 headgroup. The most important atoms in Span 60 are O28 and O29 atoms with strong H-bond interactions with the O1, O3, and O4 atoms of the DFX molecule.

2.2. Physicochemical Characterization of DFX-Niosome. In this study, pH-responsive DFX-niosomal vesicles were prepared and characterized in order to develop a carrier system for cancer therapy. Niosomes were observed through a 100× objective or a 40× objective on an optical microscope before the sonication and filtration procedure. Figure 3 shows

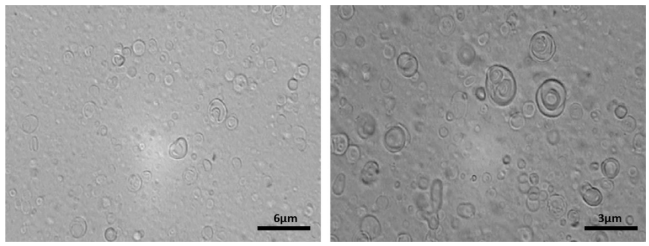

Figure 3. Optical microscopy imaging of pH-responsive DFX-niosome before sonication and filtration procedure.

niosome suspensions diluted in an external medium and studied by optical microscopy, which revealed niosomes with dimensions of micrometers. The majority of the niosomes were round or somewhat asymmetrical, with multilamellar vesicles. Because of the difference in the refractive indices of the interior and exterior media, the borders of the lipid vesicles appeared as comparatively thick and dark bands.[50]

To manufacture small niosomes with homogeneous size and dispersity and to reduce aggregation, a sonication and filtration procedure was carried out. The morphology, size, z-potential, and PDI of the niosome samples were then determined. The hydrated medium containing niosomal DFX is shown in Figure 4A. It has a milky white appearance without any aggregation.

TEM analysis (Figure 4B) demonstrated that the vesicles in the niosome formulation are spherically formed. Furthermore, with a PDI value of 0.12 ± 0.09, the size of the DFX-niosome was observed to be reduced to 107 ± 2 nm (Figure 4C). This clearly shows that sonication and filtration are excellent post-sizing reduction techniques. Based on many studies, nano-carrier size is an essential factor in tumor tissue penetration (independent of the dosing mode) and cell uptake.[51]

Because of the non-uniform charge distribution at the particle surface, the aggregation mechanism and the creation of stable formulations result from a balance between electrostatic repulsion and short-range effective attraction interactions.[52,53] The zeta potential is a relationship between the mobility and

https://doi.org/10.1021/acsomega.1c03816
ACS Omega 2021, 6, 24218−24232

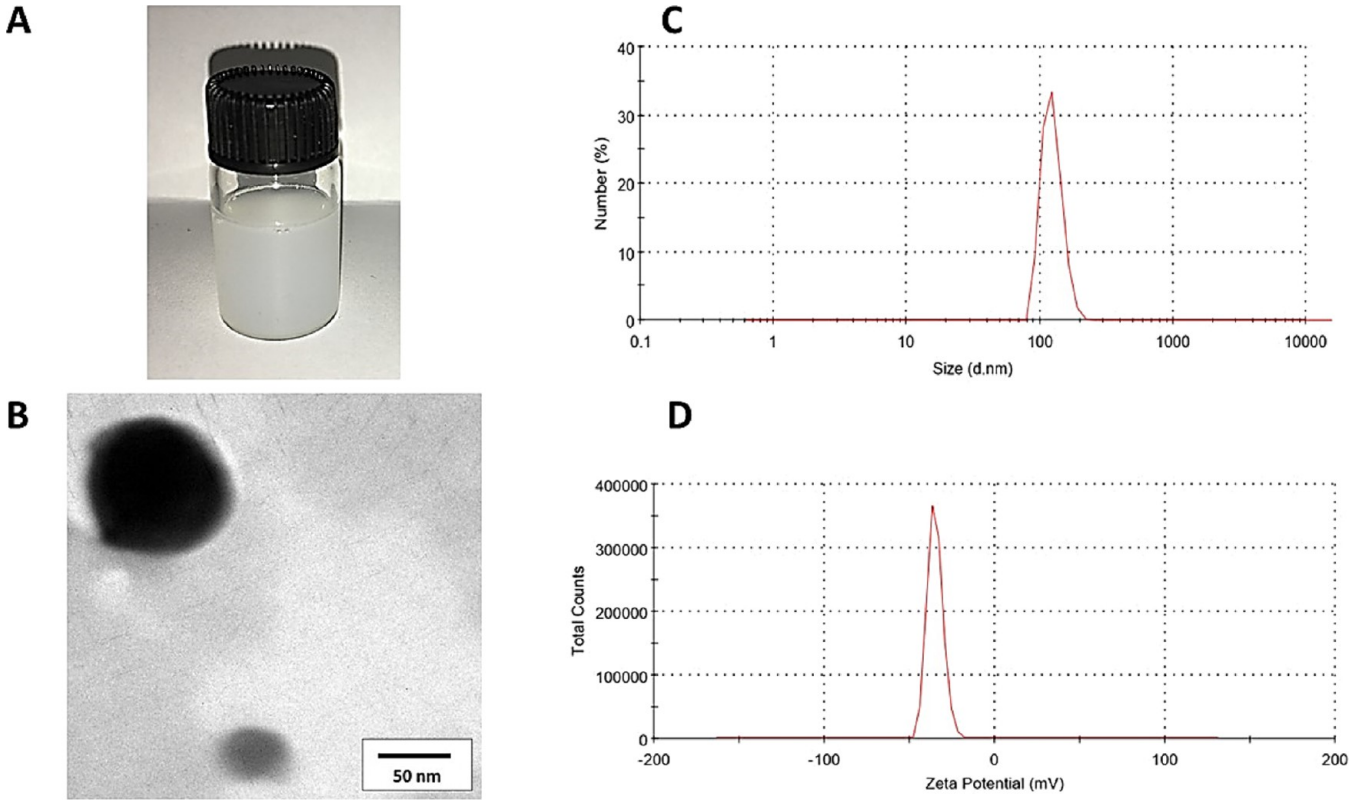

Figure 4. (A) Physical appearance, (B) transmission electron microscopy (TEM) image, (C) size distribution, and (D) zeta potential of pH-responsive DFX-loaded niosomes.

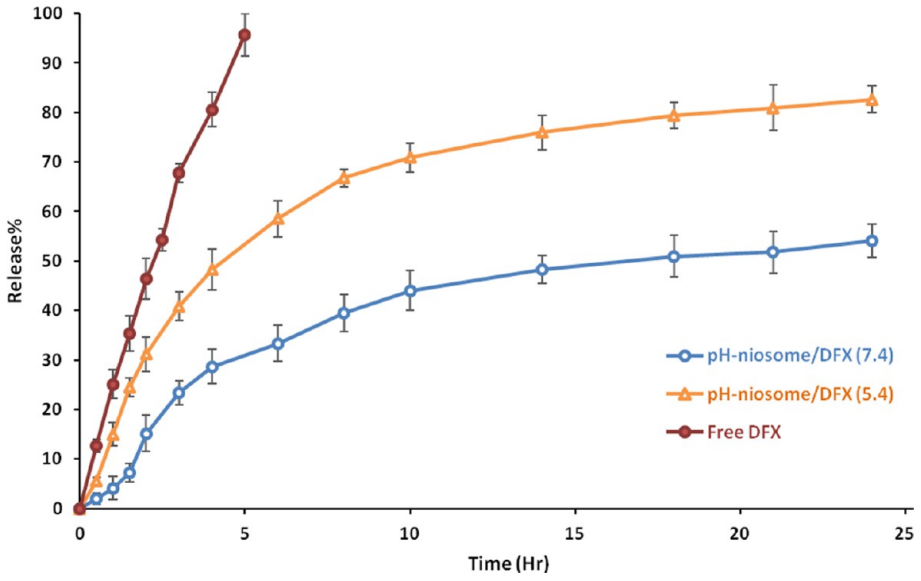

Figure 5. *In vitro* release curve of pH-responsive DFX-niosomes at pH 5.4 and 7.4 in phosphate buffer at 37 °C (mean ± SD, n = 3).

interaction of colloidal particles that shows system stability. A stable colloid system will typically have a zeta potential greater than 30 mV (it can be positive or negative).[54] The zeta potential of the prepared pH-responsive DFX-niosomes was obtained as −29.1 ± 1.15 mV (Figure 4D).

The average vesicle diameters were determined from the DLS measurement as about 107 ± 2 nm that were comparable with those obtained by TEM analysis. DLS is more accurate because the number of analyzed particles by TEM is much smaller. Although the mechanism of these two methods is different, the obtained data were in accordance with each other.

2.3. Entrapment Efficiency. The total drug used during the preparation of niosomes was 200 ppm of DFX. Therefore, using the formula, the encapsulation efficiency of pH-responsive niosome was found to be 84.2 ± 2.6% (the concentration of DFX in niosomal suspension is 168 ppm). This concentration is helpful to achieve the therapeutic efficacy.[55]

https://doi.org/10.1021/acsomega.1c03816
ACS Omega 2021, 6, 24218−24232

2.4. *In Vitro* Release Experiment. The dialysis method was used to assess *in vitro* drug release from encapsulated niosomes. Figure 5 depicts the *in vitro* release behavior of free DFX and pH-responsive niosomal DFX (pH 5.4 and 7.4) at 37 °C in phosphate-buffered saline (PBS). The drug release rate of niosomes at pH 5.4 is faster than pH 7.4, indicating that the formulation is pH responsive. The addition of CHEMS to the niosomes results in increasing the rate of drug release from the niosomes. Furthermore, the free drug had the highest release rate, but the rate of release from loaded niosomes was less than 40%. This supports the idea that the noisome bilayer works as a barrier against the diffusion of DFX. DFX was efficiently entrapped in the niosomes due to the hydrophobic long alkyl chains of the surfactants acting as a barrier.

Table 3 shows the regression parameters (i.e., the regression coefficients (R^2) and the release kinetic equation) used to fit the *in vitro* release data to several kinetic models. For both pHs, release measurements revealed a strong correlation with Higuchi kinetics. The release exponent (n) for all of the release data was found to be in the range of 0.43−0.89, indicating that the anomalous mode of drug transport is predominated. The combination of the diffusion and erosion mechanisms determines the release mechanism in this case.

Table 3. Kinetic Models of DFX Released from pH-Responsive Niosomes in pH 7.4 and 5.2

kinetic model	pH	equation	R^2
zero order	7.4	$y = 0/0353x + 12/555$	0.8109
	5.2	$y = 0/0484x + 27/08$	0.7752
first order	7.4	$y = 0/0007x + 0/9659$	0.5428
	5.2	$y = 0/0005x + 1/3535$	0.5256
Higuchi	7.4	$y = 1/6731x - 2/9191$	0.9322
	5.2	$y = 2/3224x + 5/3056$	0.9122
Korsmeyer and Peppas	7.4	$y = 0/8248x - 0/7038$	0.8979
	5.2	$y = 0/613x + 0/11$	0.8858

2.5. Cell-Killing Effects of Niosomal DFX. Treatment of cancerous and non-cancerous cells with an escalating concentration of free and encapsulated DFX-induced concentration-dependent toxicity after 48 h (Figure 6). Unloaded niosomes did not exhibit cytotoxic effects against these cell lines ($P > 0.05$ compared with untreated cells). The percentage of dead Hela cells treated with 0.781, 1.562, 3.125, 6.25, 12.5, 25, and 50 μg/mL of niosomal DFX was 11.82, 19.70, 39.21, 66.56, 70.87 76.77, and 92.16%, respectively, while these percentages were 17.15, 31.0, 55.36, 70.23, 80.44, 86.11, and 91.14% for MCF7 cells, respectively. The IC50 values of free DFX were 17.37, 33.50, and 36.21 μg/mL in HUVEC, MCF7, and Hela cell lines, respectively. In the meantime, these values were 10.81, 3.018, and 5.041 μg/mL for HUVEC, MCF7, and Hela cells exposed to niosomal DFX, respectively, in the given time period.

Despite having few rounded cells, untreated cells had a standard morphology, intact cell membrane, and were confluent. Exposing MCF7 cells (Figure 7) and Hela cells (Figure 8) to 0.781, 3.125, 12.5, and 50 μg/mL of free DFX did not cause any noticeable morphological alteration. In contrast, exposure of MCF7 (Figure 7) and Hela cells (Figure 8) to low concentrations (<12.5 μg/mL) of niosomal DFX

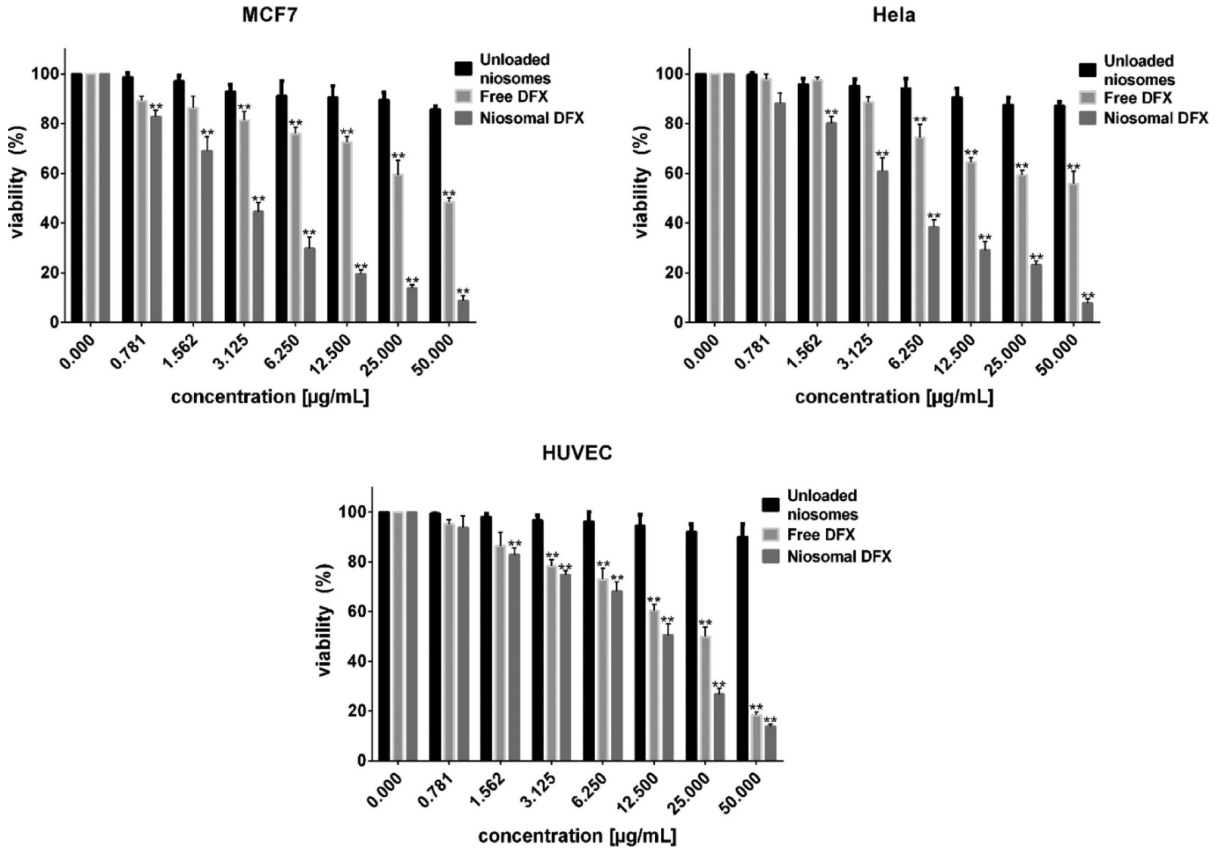

Figure 6. Cytotoxic effects of unloaded niosomes and free and niosomal DFX on malignant (MCF7 and Hela) and normal (HUVEC) human cells evaluated via the MTT assay. (**$P < 0.05$ compared with untreated cells).

https://doi.org/10.1021/acsomega.1c03816
ACS Omega 2021, 6, 24218−24232

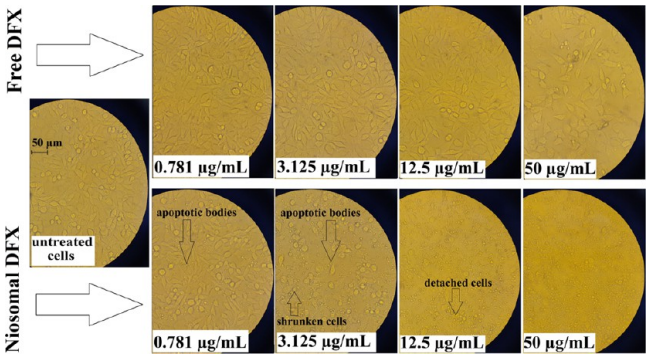

Figure 7. Morphological examination of MCF7 cancer cells treated with different concentrations of free and niosomal DFX for 48 h.

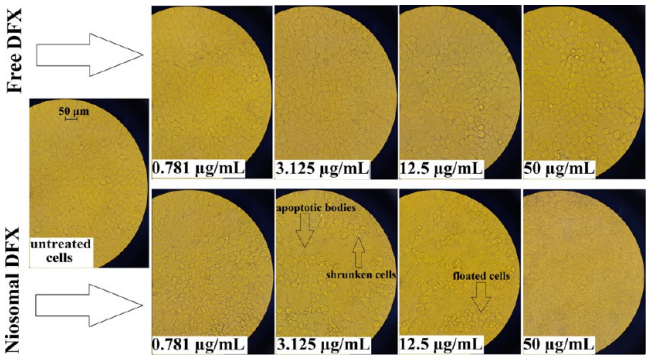

Figure 8. Morphological examination of Hela cancer cells treated with different concentrations of free and niosomal DFX for 48 h.

induced cell shrinkage and formation of apoptotic bodies. With higher concentrations of niosomal DFX (>12.5 μg/mL), cancerous cells were detached from the bottom of the plates and floated in the culture media.

2.6. Encapsulation of DFX in Niosomes Did Not Enhance the Caspase-3 Activity. Apoptosis is a type of cell death orchestrated by a large family of cysteine proteases known as caspases. Among these endoproteases, three of them (i.e., caspase-3, caspase-6, and caspase-7) coordinate to the execution phase of apoptosis via cleaving several structural and repair proteins.[56] It has been documented that activated caspase-3 activates or inactivates its substrates, resulting in the generation of a cascade of signaling events that controls cell death. Hence, activation of this caspase contributes to the destruction of cellular structures, including degradation of cytoskeletal proteins, DNA fragmentation, and appearance of distinct morphological features of apoptosis.[57] With this background, we determined caspase-3 activity in Hela cells in a time-dependent manner. *Caspase-3* is absent in MCF7 cells because of a 47-bp deletion in exon 3 of the *caspase-3* encoding gene.[58] Compared with control cells, treatment with free and encapsulated DFX significantly increased caspase-3 activity after 3, 6, 12, and 24 h, reaching the maximum at 6 h ($P < 0.05$). As shown in Figure 9, we found no significant difference between the ability of free and encapsulated drugs in activating caspase-3 ($P > 0.05$ between free DFX and niosomal DFX).

2.7. Biochemical Findings. The effects of intraperitoneal injections of free DFX and liposomal DFX on serum biochemical parameters are shown in Table 4. In the current experimental study, 56 adult Wistar male rats were divided into 7 groups and received intraperitoneal injections of different doses of free DFX and niosomal DFX. Eight weeks of

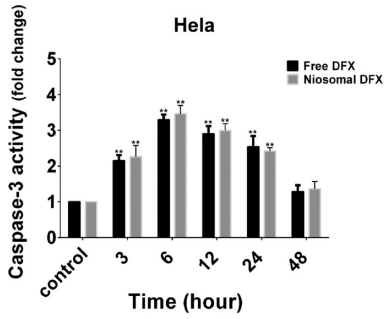

Figure 9. Effects of free and niosomal DFX on caspase-3 activity in Hela cells. (**$P < 0.05$ compared with untreated cells).

intraperitoneal administrations of free DFX at a dose of 2.5 mg/kg caused a significant increase in serum AST and serum ALT levels ($P < 0.01$ and $P < 0.001$, respectively). Serum BUN and creatinine levels also increased following treatment with a 2.5 mg/kg dose of free DFX ($P < 0.05$ and $P < 0.001$, respectively). There was also a significant increase in liver MDA content of rats treated 2.5 mg/kg dose of free DFX ($P < 0.05$). Intraperitoneal injection of DFX (5 mg/kg) caused a significant increase in serum ALT and AST ($P < 0.001$ and $P < 0.01$, respectively). The serum creatinine and blood urea nitrogen levels increased in rats treated with a 5 mg/kg dose of free DFX compared to control animals ($P < 0.001$ and $P < 0.05$, respectively). Treatment with the 10 mg/kg dose of free DFX significantly increased the serum biochemical parameters ($P < 0.001$, for all).

Intraperitoneal injection of niosomal DFX at 0.25 dose had no significant effect on liver MDA, AST, ALT, serum creatinine, and serum BUN compared to untreated rats ($P > 0.05$). Treatment with a 5 mg/kg dose of niosomal DFX caused a significant increase in serum creatinine ($P < 0.05$); however, other parameters remained unchanged.

On the other hand, administration of niosomal DFX at the highest dose (10 mg/kg) significantly increased serum creatinine ($P < 0.05$), serum BUN ($P < 0.001$), and serum liver enzymes compared to the control rats ($P < 0.01$). Treatment with niosomal DFX (10 mg/kg) significantly increased liver MDA levels of rats ($P < 0.001$).

2.8. Histopathological Results. Renal histopathological investigations of kidney sections stained with hematoxylin–eosin (H&E) at the end of the experiments showed extensive morphological changes of rat kidneys receiving free DFX (Figure 10A–G). Microscopic investigations of control rats indicated healthy kidney histopathology, normal glomerular feature, and normal cells in the kidneys of control rats (Figure 10A). Rats treated with 2.5 and 5 mg/kg of niosomal DFX showed normal histopathology (Figure 10B,C). The kidneys of rats treated with niosomal DFX at a dose of 10 mg/kg exhibited signs of histopathological injury such as narrowing of proximal tubules (Figure 10D). Microscopic investigations of kidney sections showed abnormal features in the kidneys of rats subjected to free DFX 2.5 mg/kg (Figure 10E). Photomicrographs of rats treated with free DFX 5 mg/kg also displayed some degree of renal damages such as bleeding, tubular swelling, and glomerular atrophy (Figure 10F). There were also some renal histopathological changes in the kidney sections of rats treated with niosomal DFX (10 mg/kg). Rats of this group presented tubular swelling and hemorrhage (Figure 10G).

https://doi.org/10.1021/acsomega.1c03816
ACS Omega 2021, 6, 24218–24232

Table 4. Effects of Free DFX and Niosomal DFX on Biochemical Parameters and Liver MDA Content of Different Experimental Groups[a]

	parameter						
treatment	control	DFX 2.5 mg/kg	DFX 5 mg/kg	DFX 10 mg/kg	DFX-niosome 2.5 mg/kg	DFX-niosome 5 mg/kg	DFX-niosome 10 mg/kg
ALT (U/L)	25.8 ± 4.7	50.6[d] ± 14.1	48.1[c] ± 10.3	58.7[d] ± 11.1	34.0 ± 10.2	35.0 ± 11.3	48.8[c] ± 6.9
AST (U/L)	85.6 ± 18.6	141.1[c] ± 39.9	145.7[d] ± 57.6	206.8[d] ± 57.6	82.3 ± 24.4	85.8 ± 14.0	161.9[d] ± 35.2
BUN (mg/dL)	12.8 ± 3.7	23.8[d] ± 2.5	22.6[d] ± 1.9	22.3[d] ± 3.8	14.5 ± 6.1	14.1 ± 4.0	22.3[d] ± 3.3
Creatinine (mg/dL)	0.54 ± 0.18	1.12[b] ± 0.48	1.0[b] ± 0.33	1.4[d] ± 0.27	0.87 ± 0.20	0.98[b] ± 0.27	1.1[b] ± 0.3
MDA(nmol/mg)	255.8 ± 56.7	434.7[b] ± 49.13	422.3[b] ± 77.8	537.6[b] ± 54.3	276.5 ± 93.8	276.7 ± 89.6	546.1[b] ± 32.6

[a]DFX: deferasirox; AST: aspartate aminotransferase; ALT: alanine aminotransferase; and BUN: blood urea nitrogen. [b]Significant with respect to control group ($P < 0.05$). [c]Significant with respect to control group ($P < 0.01$). [d]Significant with respect to control group ($P < 0.001$).

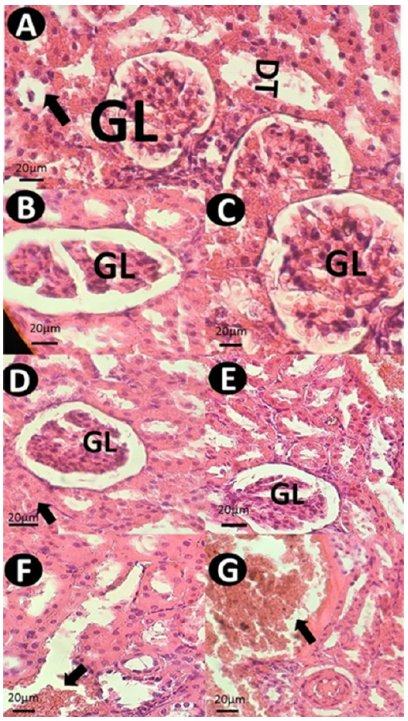

Figure 10. Kidney histopathology of control and experimental groups. (A) Normal kidney histopathology of control rats; (B) normal features in the kidneys of rats treated with 2.5 mg/kg of niosomal DFX; (C) normal histology of kidneys of rats treated with 5 mg/kg of niosomal DFX; (D) some degree of renal damages including tubular swelling in rats treated with 2.5 mg/kg of niosomal DFX (arrow); (E) abnormal features in the kidneys of rats subjected to free DFX 2.5 mg/kg; (F) photomicrograph of a rat treated with 5 mg/kg of free DFX, some degree of renal damages including hemorrhage (arrow), tubular swelling, and glomerular atrophy. (G) Histopathological changes such as hemorrhage in rats treated with 10 mg/kg of niosomal DFX including hemorrhage (arrow).

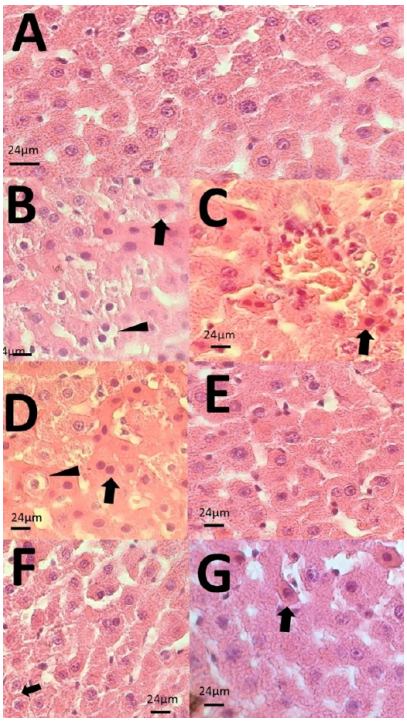

Figure 11. Liver histopathology of control and experimental groups. Hematoxylin–eosin (H&E) staining. (A) Normal liver micrograph of control rats; (B) necrosis (arrow) and fatty change (arrow head) in the liver of rats treated with DFX 2.5 mg/kg; (C) normal histology of liver of rats treated with free DFX 5 mg/kg; (D) some degree of liver damages including cytoplasmic swelling in rats treated with free DFX 10 mg/kg (arrowhead); (E) liver histopathology of liver of rats subjected to free DFX 0.25 niosome mg/kg showing normal appearance; and (F) photomicrograph of a rat treated with niosomal DFX 5 mg/kg signs of mild liver damage including cytoplasmic vacuolation. (G) Some degree of histopathological changes including necrosis (black arrow) in rats treated with DFX niosome 10 mg/kg.

Liver histopathological investigation of animals showed morphological changes in rats treated with niosomal and free DFX. Histopathological examination presented normal liver morphology of control rats (Figure 11A). The liver of rats treated with DFX 2.5 mg/kg showed necrosis and fatty change (Figure 11B). Rats treated with DFX 5 mg/kg also showed necrosis (Figure 11C). Rats treated with DFX 10 mg/kg showed signs of liver damages such as hepatocyte swelling (Figure 11D). There were no abnormal features in the liver of rats subjected to free DFX 0.25 niosome mg/kg ((Figure 11E). Photomicrograph of a rat treated with 5 mg/kg of free DFX produced some degree of liver damages. Histopathological investigations of rats of this group revealed signs of mild liver damage (Figure 11F). There were also histopathological changes such as necrosis and cytoplasmic ballooning [in rats treated with niosomal DFX 10 mg/kg (Figure 11G)].

3. DISCUSSION

Applications of nanotechnology have emerged with the increasing need of nanoparticle uses in various fields.[59,60] In this study, the APL and thickness of niosome bilayer were evaluated by MD simulation. Based on our findings, the APL of

https://doi.org/10.1021/acsomega.1c03816
ACS Omega 2021, 6, 24218−24232

Span 60 reached 22.26 ± 0.1 Å^2 at the end of simulation, which has an excellent consistency with the experimental value. Insertion of Tween 60 and ergosterol to the bilayer model with an average APL of 22.82 ± 0.1 and 26.08 ± 0.1 Å^2, respectively, does not affect the bilayer's expansion. The mass density profile of the bilayer inserted in water revealed that the Span 60 headgroup, compared to Tween 60 intended to reside at the water interface. In addition, based on this simulation, the presence of ergosterol causes the non-zero mass densities headgroup of both Span 60 and Tween 60 at the center of the bilayer due to the substantial interactions with ester or hydroxyl groups of these species. Also, we investigated the main interactions of DFX with the lipid bilayer components. According to this investigation, the main interaction between DFX and bilayer is strong hydrogen bonding with the Tween 60 headgroup. Our finding also revealed that the DFX molecules made substantial hydrogen bonds with the Tween 60 headgroup through its oxygen atoms in the 4-carboxyphenyl group at position 1 and 2-hydroxyphenyl groups at position 5. Based on our results from MD simulation, the Span 60 headgroup made the weaker interaction with DFX through the 4-carboxyphenyl group at position 1 and 2-hydroxyphenyl groups at positions 3 and 5.

Moreover, we compared the cytotoxic effects of free and encapsulated DFX in cancerous and non-cancerous cells. Based on our findings, niosomal DFX showed a safer profile in normal human cells compared to cancerous cells (higher IC50). This is promising because, nowadays, nanotechnology-based strategies are focused on limiting the adverse drug side effects of drugs on healthy cells/tissues.[61,62] Meanwhile, in cancerous cells, niosomal DFX exhibited a much desirable cytotoxic activity than free DFX, indicated by lower IC50 in both cell lines. Among the cancerous cells, MCF7 cells were more sensitive to encapsulated DFX (IC50 = 3.018 and 5.041 μg/mL for MCF7 and Hela cells, respectively). Compared with free DFX, niosomal DFX induced evident morphological changes, including cell shrinkage and appearance of apoptotic bodies, which mainly occurred during apoptotic cell death. To determine if treatment with niosomal DFX induces cell death in a caspase-dependent manner, we examined caspase-3 activity in Hela cancer cells. We found that there is no marked difference between both forms of DFX in activating caspase-3. Kamihara et al. reported that DFX induces apoptosis via inhibiting proline-rich tyrosine kinase 2 (Pyk2), which is highly expressed in osteoclasts and is established to enhance the proliferation of multiple myeloma cells.[63,64] Our results agree with Kamihara's findings, suggesting that apoptosis might be the primary cell death mechanism triggered in response to DFX. In another study, Shapira and colleagues demonstrated that DFX selectively induces cell death in leukemic cells, possibly through induction of oxidative stress, which might be a caspase-independent cell death mechanism.[65] It has been shown that caspase-3 plays a pivotal role in apoptotic execution. In this respect, downregulation or deficiency of caspase-3 has been associated with several types of tumors.[66,67] Hence, activating caspase-3 is a beneficial approach to induce apoptotic cell death in cancer cells.[68] According to our results, although it seems that DFX induces cell death through a caspase-3-dependent pathway, more studies are required to elucidate the primary cell death mechanism activated by our formulation. Our previous study showed that DFX-loaded nanomicelles exhibited greater cytotoxic effects than free DFX in HepG2 liver cancer cells and lower toxicity in normal HUVEC cells.[1] In agreement with our previous findings, niosomal DFX showed more desirable tumor-killing activity than free DFX in cancer cells derived from breast and cervical tissues. Several niosomal formulations have recently shown promising results as a novel drug delivery system to combat cancer.[69−71]

Results of the *in vivo* study showed that chronic treatment with free DFX could induce significant changes in serum biochemical parameters of rats. Treatment with free DFX also induced histopathological changes in the liver and kidney of rats. These results showed that free DFX could easily penetrate through kidneys and tissues. The current results also showed the long-term toxicity of niosomal DFX in rats. Previous studies have shown that VPA could induce long-term histopathological changes in rats. The results of the current study were in line with previous studies. Few data are available regarding the chronic toxicity of niosomal DFX. The current results also suggest that the niosomal DFX could induce biochemical and histopathological changes at high doses. In this work, both free DFX and niosomal DFX showed toxic effects at high doses, suggesting the dose-dependent toxicity of niosomal DFX and free DFX.

On the other hand, 8 weeks of intraperitoneal injections of free DFX showed more toxic effects compared to niosomal DFX. This effect could be due to the biochemical properties of niosomal DFX including better solubility. It seems that the better solubility of niosomal DFX is responsible for the lower toxicity of these nanomaterials. The histopathological results showed that both free DFX and niosomal DFX could induce histopathological changes in the liver and kidneys of rats. The results of histopathological investigations indicate that both free and niosomal forms of DFX can penetrate different tissues.

4. CONCLUSIONS

Niosome modified with ergosterol and CHEMS was loaded with DFX and evaluated for anticancer effect. Results showed that the prepared formulation has a nanometric range, negative zeta potential, high EE %, and pH-responsive ability. Also, the theoretical investigation revealed that the major interaction of DFX loaded in niosome is due to its 4-carboxyphenyl group at position 1 and 2-hydroxyphenyl groups at position 5 with Tween 60. Developed formulations induced caspase-3-dependent cell death in cancerous cells. *In vivo* data demonstrated that DFX and free DFX could induce biochemical and histopathological changes at high doses; however, free DFX showed more toxic effects than niosomal DFX. This effect could be due to the biochemical properties of niosomal DFX and solubility. Therefore, this might provide a therapeutic option to combat cancer. Yet, the safety of our formulation in healthy cells/organs should be further studied.

5. MATERIALS AND METHODS

5.1. Chemicals, Assay Kits, and Cell Line. DFX, penicillin, streptomycin, 3-(4,5-dimethylthiazol-2-yl)-2, 5-diphenyltetrazolium bromide (MTT), Span 60, Tween 60, and ergosterol were obtained from Sigma-Aldrich (Steinheim am Albuch, Germany and St Louis, MO, USA). PBS, trypan blue, L-glutamine, 0.25% trypsin−ethylenediaminetetraacetic acid solution, and dimethyl sulfoxide (DMSO) were procured from INOCLON (Tehran, Iran). Fetal bovine serum (FBS) and Dulbecco's modified Eagle's medium (DMEM) were purchased from Gibco (Grand Island, NY, USA). Cholesterol

https://doi.org/10.1021/acsomega.1c03816
ACS Omega 2021, 6, 24218−24232

Scheme 1. Schematic Representation for pH-Responsive DFX-Niosome and Its *In Silico*, *In Vitro*, and *In Vivo* Evaluations

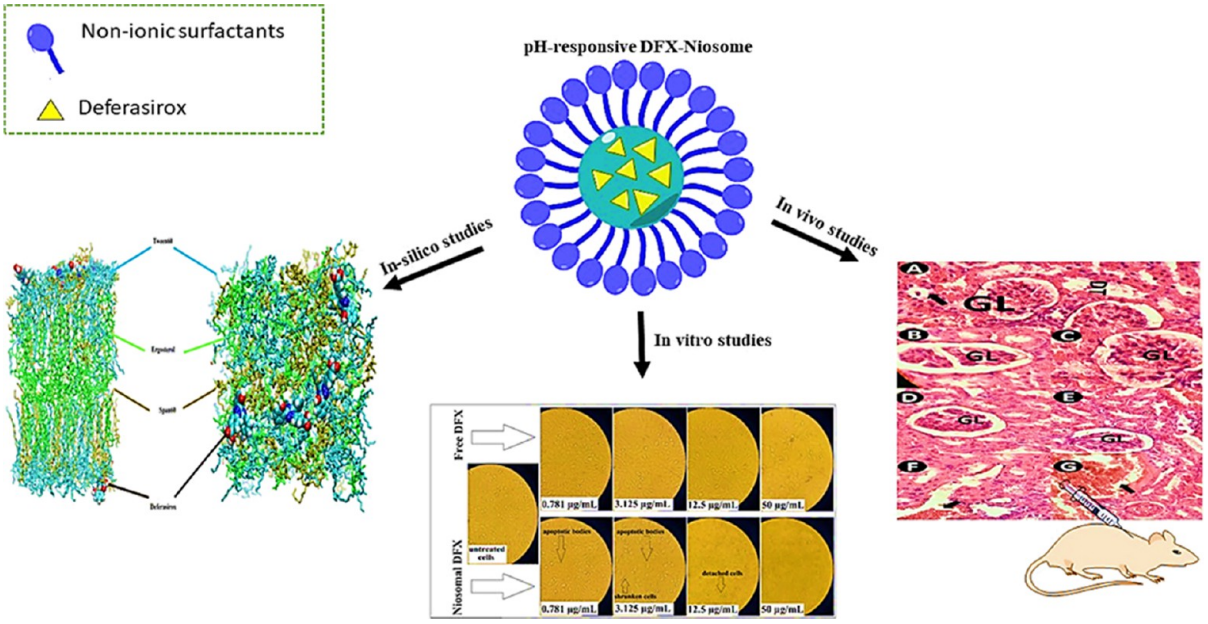

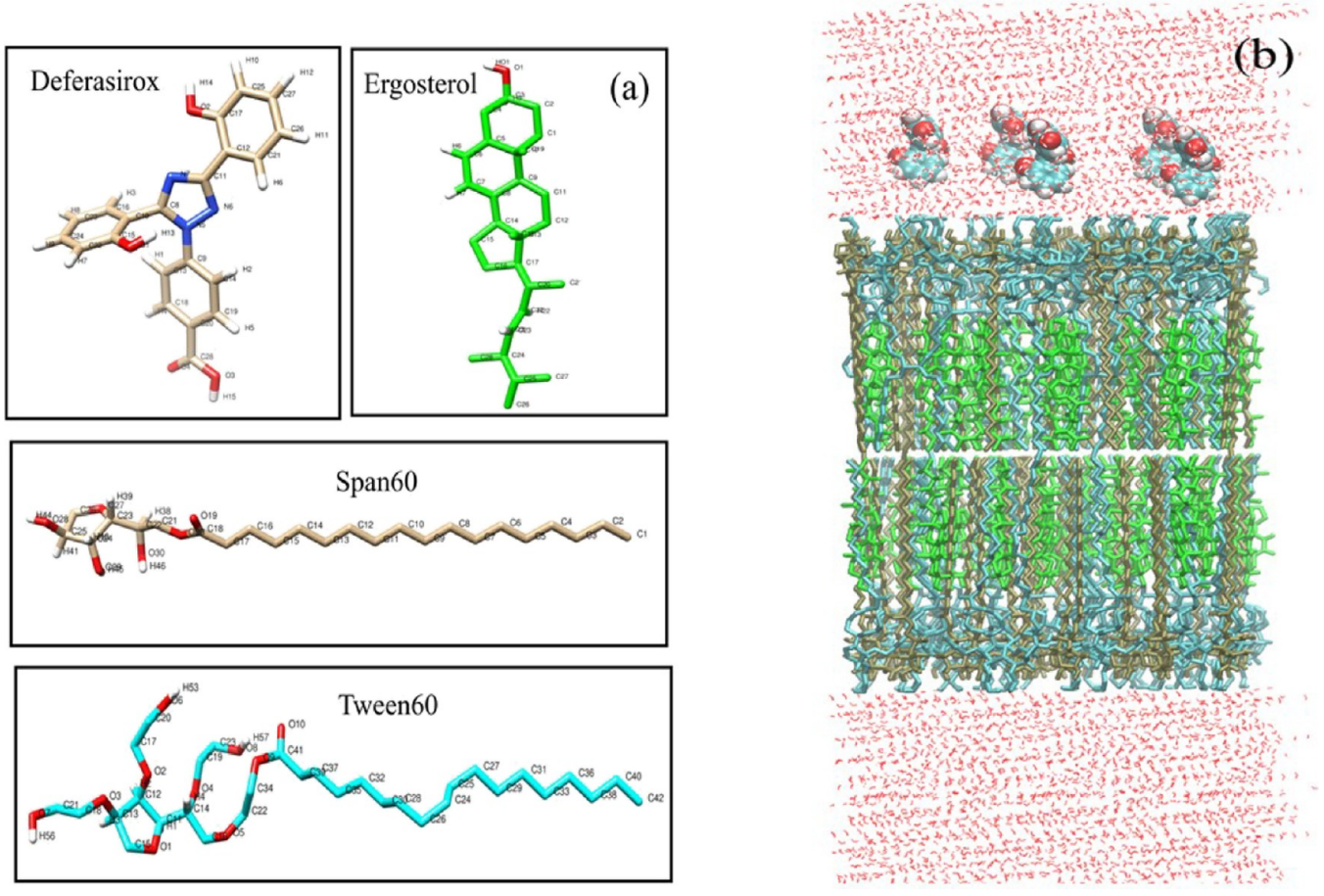

Figure 12. (a) Molecular structure of deferasirox, Span 60, Tween 60, and ergosterol with the numbering of atoms based on the amber nomenclature. (b) Starting structure of niosome bilayer containing DFX drugs at the top. Span 60, Tween 60, and ergosterol lipids are colored as tan, cyan, and green, respectively. The DFX molecules are represented as the space-filling model.

hemisuccinate (CHEMS) was obtained from Avanti Polar, USA. Caspase-3 assay kit was procured from R&D (R&D Systems Co., Grodig, Germany). Michigan Cancer Foundation-7 (MCF-7) breast cancer cells, Hela cervical cancer cells, and normal human umbilical vein endothelial cells (HUVECs) were obtained from the cell bank of Pasteur Institute of Iran

https://doi.org/10.1021/acsomega.1c03816
ACS Omega 2021, 6, 24218−24232

(Tehran, Iran) and grown in DMEM culture medium supplemented with the antibiotic mixture (50 U/mL of penicillin and 50 μg/mL of streptomycin) and 10% heat-inactivated FBS. Cells were incubated at 37 °C in a humidified atmosphere with 5% CO_2.

5.2. Preparation of DFX-Loaded Niosomes. Niosomes were prepared using the thin-film hydration method.[72] Span 60, Tween 60, ergosterol, and CHEMS, in molar ratios of 3:3:3:1, was mixed to prepare pH-responsive niosomes. In addition, 200 ppm of DFX was used for DFX-loaded formulation. In a general procedure, the lipid mixtures (50 mg/mL) along with DFX were dissolved in chloroform. Then, the organic solvent was evaporated at 60 °C, 15 min, and 180 rpm using a rotary vacuum evaporator (Laborota 4003, Heidolph, Germany) to produce a thin lipid film. The thin film was then hydrated for 30 min at 60 °C with 5 mL of ultrapure water that pre-warmed to 60 °C. The hydration step took place in the presence of some glass beads 4 mm in diameter for better homogenization of formulations. The unencapsulated drug was separated from the encapsulated one by centrifugation at 15,000 rpm for 60 min (5415D, Eppendorf, Germany). The formed pellets were washed twice with deionized water and recentrifuged again for 1 h at 15,000 rpm. Resulted formulations were sonicated with an ultrasonic bath sonicator (Thermo Fisher Scientific, USA) and then filtered with 0.45 and 0.22 μm polycarbonate membrane filters (Sartorius AG, Göttingen, Germany). The obtained niosome dispersion was characterized in terms of entrapment efficiency, particle size analysis, and morphological studies. A schematic representation of pH-responsive DFX-niosomes and different studies is given in Scheme 1.

5.3. Simulation. *5.3.1. System Setup and Simulation Details.* First, the structures of Span 60, Tween 60, ergosterol, and deferasirox (DFX) molecules were retrieved from PUBCHEM and then geometrically optimized using B3LYP/6-3G(d,p) calculations. A bilayer niosome containing 35:35:30 molar ratio of Span 60/Tween 60/ergosterol was built using the CELL microcosmos 2.2 software (the optimized structures are shown in Figure 12).[73] This bilayer niosome contained 82 Span 60, 80 Tween 60, and 70 ergosterol molecules in each leaflet, leading to 230 molecules in total. Span 60, Tween 60, and ergosterol molecules were randomly placed in a box area of 4.50 nm × 4.50 nm with the hydrophilic heads and hydrophobic part placed inversely toward each other in the box.

As shown in Figure 12, 5 numbers of DFX molecules were inserted in the upper leaflet of the bilayer to investigate the interactions of these molecules with the niosome bilayer. The final structure was solvated in a SPC/E water box as this model can reproduce the surface tension of the water more accurately.[74] The force filed parameters, and electrostatic charge distributions of all molecules, were obtained from the ATB server[75] based on Gromos87[76] and Gromos96 54A7 force field.[77] To avoid the unexpected overlap between atoms in the constructed niosome bilayer, the whole system was subjected to energy minimization using the steepest descent algorithm. A short simulation annealing was conducted in 500 K for 100 ps to remove the remaining clashes among atoms in the box. The system was subsequently subjected to the *NVT* stimulation run for 500 ps at 298 K to equilibrate the system's temperature. The choice of this temperature corresponds to the optimal conditions for the formation of niosome vesicles that show the highest stability.[78] In this step, Span 60, Tween 60, and ergosterol were coupled together to the v-rescale thermostat with a coupling constant 0.1 ps while the water and DFX were coupled separately. The resulted configuration was then subjected to 10 ns of *NPT* simulation using the Berendsen barostat[79] with semi-isotropic coupling to maintain the temperature and pressure of the system at 298 and 1 bar, respectively. The periodic boundary conditions were applied in all three directions. Bond constraints were applied using the LINCS algorithm,[80] and the electrostatic interactions were calculated using the fast particle mesh Ewald (PME) method.[81] The cutoff for the Coulomb and van der Waals interactions was assigned to 1.5 nm. The systems were simulated for a 40 ns production run in the Gromacs 2020.1 package.

5.4. Characterization of pH-Responsive Vesicular DFX. *5.4.1. Size and Zeta Potential by DLS.* Using the Zetasizer Nano ZS, the particle size (nm), zeta potential (mV), and polydispersity index (PDI) of the niosomes were determined by the DLS method (Malvern, Helix, UK). At a temperature of 25 °C, the analysis was carried out with a He−Ne laser (wavelength of 633 nm) and a detector angle of 90°. Before analysis, the samples were diluted in deionized water with a dilution factor of 1:20. The measurements of size and zeta were done in triplicate, and the results are expressed as mean SD (nm and mV, respectively).

5.4.2. Morphology by Optical Microscopy and TEM. The prepared niosomal vesicles (before sonication and filtration procedure) were characterized for morphology, that is, shape uniformity and lamellarity, employing an optical microscope (ICC50 W, Germany).

The morphology of the niosomes (after sonication and filtration) was characterized using a transmission electron microscope (EM10C, Zeiss, Germany) operating at 120 kV. To decrease the concentration of vesicles, the niosomes were diluted with deionized water at a dilution rate of 1:20. On a copper grid, a drop of diluted sample was deposited and allowed to dry at room temperature under air. Phosphotungstic acid was used to stain the grid. Filter paper was used to remove excess liquid, which was then dried in a desiccator. The grid was then installed in the device, and images at various magnifications were obtained.

5.5. Determination of Encapsulation Efficiency (EE %). After the separation procedure, the percentage of drugs encapsulated was calculated. A UV−visible spectrophotometer (Agilent Technologies, Cary 50, USA) was used to measure the concentration of DFX in the supernatant in triplicate at 300 nm. The difference between the total drug and the drug content in the supernatant was used to calculate EE %.

5.6. *In Vitro* Drug Release Studies. To assess the release response of pH niosome, an *in vitro* release study was performed in two different PBS media (pH 5.4 and 7.4). Three dialysis bags were prepared containing free DFX as the control and DFX in pH-responsive niosomes (pH 5.4 and 7.4). Briefly, 1 mL of each loaded formulation was placed in a dialysis bag (12 kDa cutoff; Sigma-Aldrich). The dialysis bags were soaked before use in distilled water at room temperature for 12 h to remove the preservative, followed by rinsing thoroughly in distilled water. The control bags (free DFX with a concentration of 200 ppm) were prepared and tested along with loaded formulations. Two ends of the dialysis bags were tightly bound and hung inside a beaker containing buffer solution (PBS buffer, pH 5.4 and 7.4). The beaker was kept on a magnetic stirrer, and stirring was maintained at 150 rpm at 37 °C with thermostatic control. Samples from buffer medium

https://doi.org/10.1021/acsomega.1c03816
ACS Omega 2021, 6, 24218−24232

were collected in time intervals up to 24 h and monitored spectrophotometrically for drug content at 300 nm. DFX release kinetics of loaded formulations was evaluated using different mathematical models (zero order, first order, and Higuchi and Korsmeyer−Peppas).[82]

5.7. Cytotoxicity and Morphological Examinations. The cytotoxic activity of free DFX and prepared niosomal DFX was assessed against cancerous (MCF-7 and Hela) and normal (HUVEC) cells using the MTT assay as previously described.[83−85] For this purpose, cells (6×10^3 cell/well) were plated in 96-well plates and stored overnight under standard conditions to attach to the flask. Increasing concentrations (0.781, 1.562, 3.125, 6.25, 12.5, 25, and 50 μg/mL) of free and niosomal DFX were added to the wells and incubated for 48 h. Untreated cells were considered as controls. At the end of the incubation period, the supernatant was discarded and 200 μL of MTT solution (0.5 mg/mL dissolved in PBS) was added to each well and further incubated for 3 h. The participated formazan crystals were then dissolved by adding 200 μL of DMSO, and absorbance (A) was read at 570 nm using a SpectraMax microplate reader (Molecular Devices, Sunnyvale, CA). Cell viability was calculated as $((A_{test} - A_{blank})/(A_{control} - A_{blank})) \times 100$. The IC50 values were calculated using GraphPad Prism software version 6.01 (GraphPad Software Inc., San Diego, California. USA). This test was repeated at least three independent times in triplicates.

For morphological evaluation, cancerous cells were exposed to 0.781, 3.125, 12.5, and 50 μg/mL of free and niosomal DFX during the same incubation period. Alterations in cell morphology were monitored using an inverted microscope (Olympus Microscope, Center Valley, PA) and imaged by a digital camera.

5.8. Caspase-3 Activation. Hela cells (3×10^5 cell/well) were plated in six-well plates and treated with 6.25 μg/mL of free and niosomal DFX for 3, 6, 12, 24, and 48 h. The relative activity of caspase-3, a frequently activated death protease, was evaluated in cells supernatant using a colorimetric commercial kit following the manufacturer's instructions. Results were expressed as fold changes.

5.9. Animal Treatments and Experimental Design. Fifty-six male adult male rats were housed under room temperature (25 °C) and 12 h light/12 h dark cycles in the laboratory animal center of the faculty of veterinary medicine, University of Zabol, Zabol, Iran. Rats had access to sterile water and a pelleted diet. For investigating the long-term toxicity of niosomal DFX, 56 male adult Wistar rats received intraperitoneal injections of free DFX and niosomal DFX at three doses of 2.5, 5, and 10 mg/kg. The experiments were performed according to the guidelines of care and the use of laboratory rodents NIH publication no. 85-23. The doses of drugs were selected based on our preliminary experiments.

5.9.1. Serum Biochemical Parameters. At the end of the experiments, blood samples were collected from retro-orbital sinus. The collected blood was centrifuged (3000 rpm for 10 min) to separate the serum. The serum samples were then sent to the clinical pathology laboratory for biochemical investigations. The serum levels of creatinine and BUN (blood urea nitrogen) were measured according to Pars Azmoon reagent kits instructions (Pars Azmoon. Co., Tehran, Iran). All biological analyses were performed using the Selectra Pro M autoanalyzer (Vital Scientific, Netherlands). A colorimetric assay was used to determine serum alanine aminotransferase (ALT) and serum aspartate aminotransferase (AST) levels.

5.9.2. Histopathological Examination. At the end of the experiments, animals were euthanized by intraperitoneal injections of 1.5% pentobarbital sodium (200 mg/kg), followed by cervical dislocation. Liver and kidney specimens were sliced and preserved in 10% neutral buffered formalin. After paraffin embedding and block making, paraffin blocks were cut into slides. The tissue sections were stained with the hematoxylin−eosin staining method. The stained tissue sections were examined under a light microscope (Tokyo, Olympus, Japan).

5.10. Statistical Analysis. The biological and histopathological data were analyzed using the SPSS software (version 16.0) and one-way analysis of variance (ANOVA). The Tukey post hoc test was used to determine the statistical difference between the experimental groups. The level of significance was set at $P < 0.05$.

AUTHOR INFORMATION

Corresponding Authors

Mohammad Reza Hajinezhad − *Basic Veterinary Science Department, Veterinary Faculty, University of Zabol, Zabol 9861335856, Iran*; Email: hajinezhad@uoz.ac.ir

Abbas Rahdar − *Department of Physics, University of Zabol, Zabol 9861335856, Iran*; orcid.org/0000-0003-4766-9214; Email: a.rahdar@uoz.ac.ir

Md. Khalid Anwer − *Department of Pharmaceutics, College of Pharmacy, Prince Sattam Bin Abdulaziz University, Alkharj 11942, Saudi Arabia*; Email: mkanwer2002@yahoo.co.in

M. Ali Aboudzadeh − *CNRS, University Pau & Pays Adour, E2S UPPA, Institut des Sciences Analytiques et de Physico-Chimie pour l'Environnement et les Matériaux, IPREM, UMR5254, 64000 Pau, France*; orcid.org/0000-0001-8829-8072; Email: m.aboudzadeh-barihi@univ-pau.fr

Authors

Mahmood Barani − *Medical Mycology and Bacteriology Research Center, Kerman University of Medical Sciences, Kerman 7616913555, Iran*

Saman Sargazi − *Cellular and Molecular Research Center, Resistant Tuberculosis Institute, Zahedan University of Medical Sciences, Zahedan 9816743463, Iran*

Fakhara Sabir − *Faculty of Pharmacy, Institute of Pharmaceutical Technology and Regulatory Affairs, University of Szeged, Szeged H-6720, Hungary*

Abbas Pardakhty − *Pharmaceutics Research Center, Nauropharmacology Research Institute, Kerman University of Medical Sciences, Kerman 7616913555, Iran*

Farshid Zargari − *Pharmacology Research Center, Zahedan University of Medical Sciences, Zahedan 9816743463, Iran; Department of Chemistry, Faculty of Science, University of Sistan and Baluchestan, Zahedan 98135674, Iran*

Complete contact information is available at: https://pubs.acs.org/10.1021/acsomega.1c03816

Funding

This study received funding from Zahedan University of Medical Sciences (Project. 10267). The *in vivo* part of the current work was supplied by the University of Zabol (grant number: 9618-15).

Notes

The authors declare no competing financial interest.

Institutional Review Board Statement: The *in vitro* part of the study was approved by Zahedan University of Medical Sciences (Ethical code: IR.ZAUMS.REC.1399.517).

■ ACKNOWLEDGMENTS

This publication was supported by the Deanship of Scientific Research at Prince Sattam Bin Abdulaziz University, Al-Kharj Saudi Arabia.

■ REFERENCES

(1) Rahdar, A.; Hajinezhad, M. R.; Sargazi, S.; Barani, M.; Bilal, M.; Kyzas, G. Z. Deferasirox-loaded pluronic nanomicelles: Synthesis, characterization, in vitro and in vivo studies. *J. Mol. Liq.* **2021**, *323*, 114605.
(2) Taghavi, F.; Saljooghi, A. S.; Gholizadeh, M.; Ramezani, M. Deferasirox-coated iron oxide nanoparticles as a potential cytotoxic agent. *MedChemComm* **2016**, *7*, 2290−2298.
(3) Taghavi, F.; Gholizadeh, M.; Saljooghi, A. S. Deferasirox loaded on fumed silica nanoparticles used in cancer treatment. *New J. Chem.* **2016**, *40*, 2696−2703.
(4) Moukalled, N. M.; Bou-Fakhredin, R.; Taher, A. T. Deferasirox: over a decade of experience in thalassemia. *J. Hematol.* **2018**, *10*, No. e2018066.
(5) Bedford, M. R.; Ford, S. J.; Horniblow, R. D.; Iqbal, T. H.; Tselepis, C. Iron chelation in the treatment of cancer: a new role for deferasirox? *J. Clin. Pharmacol.* **2013**, *53*, 885−891.
(6) Ford, S.; Obeidy, P.; Lovejoy, D.; Bedford, M.; Nichols, L.; Chadwick, C.; Tucker, O.; Lui, G.; Kalinowski, D.; Jansson, P.; Iqbal, T.; Alderson, D.; Richardson, D.; Tselepis, C. Deferasirox (ICL670A) effectively inhibits oesophageal cancer growth in vitro and in vivo. *Br. J. Pharmacol.* **2013**, *168*, 1316−1328.
(7) Choi, J. H.; Kim, J. S.; Won, Y. W.; Uhm, J.; Park, B. B.; Lee, Y. Y. The potential of deferasirox as a novel therapeutic modality in gastric cancer. *World J. Surg. Oncol.* **2016**, *14*, 77.
(8) Bedford, M. R. A Role for Deferasirox as an Anti-neoplastic and Chemosensitising Agent in Gastrointestinal Cancer. Ph.D., University of Birmingham, 2015.
(9) Vazana-Barad, L.; Granot, G.; Mor-Tzuntz, R.; Levi, I.; Dreyling, M.; Nathan, I.; Shpilberg, O. Mechanism of the antitumoral activity of deferasirox, an iron chelation agent, on mantle cell lymphoma. *Leuk. Lymphoma* **2013**, *54*, 851−859.
(10) Gao, Y.; Glennon, B.; Kamaraju, V. K.; Hou, G.; Donnellan, P. Dissolution kinetics of a BCS class II active pharmaceutical ingredient. *Org. Process Res. Dev.* **2018**, *22*, 328−336.
(11) Yang, Y.; Chen, H.; Zou, X.; Shi, X.-L.; Liu, W.-D.; Feng, L.; Suo, G.; Hou, X.; Ye, X.; Zhang, L.; Sun, C.; Li, H.; Wang, C.; Chen, Z.-G. Flexible carbon-fiber/semimetal Bi nanosheet arrays as separable and recyclable plasmonic photocatalysts and photoelectrocatalysts. *ACS Appl. Mater. Interfaces* **2020**, *12*, 24845−24854.
(12) Zhang, L.; Zheng, J.; Tian, S.; Zhang, H.; Guan, X.; Zhu, S.; Zhang, X.; Bai, Y.; Xu, P.; Zhang, J.; Li, Z. Effects of Al3+ on the microstructure and bioflocculation of anoxic sludge. *J. Environ. Sci.* **2020**, *91*, 212−221.
(13) Zhang, M.; Zhang, L.; Tian, S.; Zhang, X.; Guo, J.; Guan, X.; Xu, P. Effects of graphite particles/Fe3+ on the properties of anoxic activated sludge. *Chemosphere* **2020**, *253*, 126638.
(14) Ehrampoush, M. H.; Moussavi, G.; Ghaneian, M.; Rahimi, S.; Ahmadian, M. Removal of methylene blue (MB) dye from textile synthetic wastewater using TiO2/UV-C photocatalytic process. *Aust. J. Basic Appl. Sci.* **2010**, *4*, 4279−4285.
(15) Malakootian, M.; Nasiri, A.; Khatami, M.; Mahdizadeh, H.; Karimi, P.; Ahmadian, M.; Asadzadeh, N.; Heidari, M. R. Experimental data on the removal of phenol by electro-H2O2 in presence of UV with response surface methodology. *MethodsX* **2019**, *6*, 1188−1193.
(16) Dong, P.; Zhang, T.; Xiang, H.; Xu, X.; Lv, Y.; Wang, Y.; Lu, C. Controllable synthesis of exceptionally small-sized superparamagnetic magnetite nanoparticles for ultrasensitive MR imaging and angiography. *J. Mater. Chem. B* **2021**, *9*, 958−968.
(17) Wang, Z.; Zhang, T.; Pi, L.; Xiang, H.; Dong, P.; Lu, C.; Jin, T. Large-scale one-pot synthesis of water-soluble and biocompatible upconversion nanoparticles for dual-modal imaging. *Colloids Surf., B* **2021**, *198*, 111480.
(18) Zhang, J.; Wang, N.; Li, Q.; Zhou, Y.; Luan, Y. A two-pronged photodynamic nanodrug to prevent metastasis of basal-like breast cancer. *Chem. Commun.* **2021**, *57*, 2305−2308.
(19) Ren, X.; Wang, N.; Zhou, Y.; Song, A.; Jin, G.; Li, Z.; Luan, Y. An injectable hydrogel using an immunomodulating gelator for amplified tumor immunotherapy by blocking the arginase pathway. *Acta Biomater.* **2021**, *124*, 179−190.
(20) Zhang, M.; Qin, X.; Xu, W.; Wang, Y.; Song, Y.; Garg, S.; Luan, Y. Engineering of a dual-modal phototherapeutic nanoplatform for single NIR laser-triggered tumor therapy. *J. Colloid Interface Sci.* **2021**, *594*, 493−501.
(21) Ni, Z.; Cao, X.; Wang, X.; Zhou, S.; Zhang, C.; Xu, B.; Ni, Y. Facile Synthesis of Copper (I) Oxide Nanochains and the Photo-Thermal Conversion Performance of Its Nanofluids. *Coatings* **2021**, *11*, 749.
(22) Miri, A.; Beiki, H.; Najafidoust, A.; Khatami, M.; Sarani, M. Cerium oxide nanoparticles: green synthesis using Banana peel, cytotoxic effect, UV protection and their photocatalytic activity. *Bioprocess Biosyst. Eng.* **2021**, *44*, 1891.
(23) Miri, A.; Sarani, M.; Khatami, M. Nickel-doped cerium oxide nanoparticles: biosynthesis, cytotoxicity and UV protection studies. *RSC Adv.* **2020**, *10*, 3967−3977.
(24) Nazaripour, E.; Mousazadeh, F.; Doosti Moghadam, M.; Najafi, K.; Borhani, F.; Sarani, M.; Ghasemi, M.; Rahdar, A.; Iravani, S.; Khatami, M. Biosynthesis of lead oxide and cerium oxide nanoparticles and their cytotoxic activities against colon cancer cell line. *Inorg. Chem. Commun.* **2021**, *131*, 108800.
(25) Sabir, F.; Qindeel, M.; Zeeshan, M.; Ul Ain, Q.; Rahdar, A.; Barani, M.; González, E.; Aboudzadeh, M. A. Onco-Receptors Targeting in Lung Cancer via Application of Surface-Modified and Hybrid Nanoparticles: A Cross-Disciplinary Review. *Processes* **2021**, *9*, 621.
(26) Fattahian, Y.; Riahi-Madvar, A.; Mirzaee, R.; Torkzadeh-Mahani, M.; Asadikaram, G.; Sargazi, G. Optimization of in vitro refolding conditions of recombinant Lepidium draba peroxidase using design of experiments. *Int. J. Biol. Macromol.* **2018**, *118*, 1369−1376.
(27) Ahmad, M. Z.; Rizwanullah, M.; Ahmad, J.; Alasmary, M. Y.; Akhter, M. H.; Abdel-Wahab, B. A.; Warsi, M. H.; Haque, A. Progress in nanomedicine-based drug delivery in designing of chitosan nanoparticles for cancer therapy. *Int. J. Polym. Mater.* **2021**, DOI: 10.1080/00914037.2020.1869737.
(28) Demirbolat, G. M.; Aktas, E.; Coskun, G. P.; Erdogan, O.; Cevik, O. New Approach to Formulate Methotrexate-Loaded Niosomes: In Vitro Characterization and Cellular Effectiveness. *J. Pharm. Innov.* **2021**, DOI: 10.1007/s12247-021-09539-4.
(29) Marzban, A.; Najafabadi, A. H.; Akbarzadeh, A.; Ardestani, M. S.; Ardestani, F.; Akbari, M. Nano-niosome particles loaded with deferoxamine for management of iron overload complications. *Front. Bioeng. Biotechnol.* **2016**, DOI: 10.3389/conf.FBIOE.2016.01.02187.
(30) Marzban, A.; Akbarzadeh, A.; Ardestani, M. S.; Ardestani, F.; Akbari, M. Synthesis of nano-niosomal deferoxamine and evaluation of its functional characteristics to apply as an iron-chelating agent. *Can. J. Chem. Eng.* **2018**, *96*, 107−112.
(31) Barani, M.; Nematollahi, M. H.; Zaboli, M.; Mirzaei, M.; Torkzadeh-Mahani, M.; Pardakhty, A.; Karam, G. A. In silico and in vitro study of magnetic niosomes for gene delivery: The effect of ergosterol and cholesterol. *Mater. Sci. Eng., C* **2019**, *94*, 234−246.
(32) Xu, X.; Bittman, R.; Duportail, G.; Heissler, D.; Vilcheze, C.; London, E. Effect of the structure of natural sterols and sphingolipids on the formation of ordered sphingolipid/sterol domains (rafts). *J. Biol. Chem.* **2001**, *276*, 33540−33546.
(33) Pencer, J.; Nieh, M.-P.; Harroun, T. A.; Krueger, S.; Adams, C.; Katsaras, J. Bilayer thickness and thermal response of dimyristoyl-

phosphatidylcholine unilamellar vesicles containing cholesterol, ergosterol and lanosterol: a small-angle neutron scattering study. *Biochim. Biophys. Acta* **2005**, *1720*, 84−91.
(34) Adams, M. L.; Kwon, G. S. Relative aggregation state and hemolytic activity of amphotericin B encapsulated by poly (ethylene oxide)-block−poly (N-hexyl-l-aspartamide)-acyl conjugate micelles: effects of acyl chain length. *J. Controlled Release* **2003**, *87*, 23−32.
(35) Caddeo, C.; Gabriele, M.; Nácher, A.; Fernàndez-Busquets, X.; Valenti, D.; Maria Fadda, A.; Pucci, L.; Manconi, M. Resveratrol and artemisinin eudragit-coated liposomes: A strategy to tackle intestinal tumors. *Int. J. Pharm.* **2021**, *592*, 120083.
(36) Tila, D.; Yazdani-Arazi, S. N.; Ghanbarzadeh, S.; Arami, S.; Pourmoazzen, Z. pH-sensitive, polymer modified, plasma stable niosomes: promising carriers for anti-cancer drugs. *EXCLI Journal* **2015**, *14*, 21.
(37) Mehta, S. Anti-cancer drugs targeting using nanocarrier niosomes-a review. *TMR Cancer* **2020**, *3*, 169−174.
(38) Baranei, M.; Taheri, R. A.; Tirgar, M.; Saeidi, A.; Oroojalian, F.; Uzun, L.; Asefnejad, A.; Wurm, F. R.; Goodarzi, V. Anticancer effect of green tea extract (GTE)-Loaded pH-responsive niosome Coated with PEG against different cell lines. *Mater. Today Commun.* **2021**, *26*, 101751.
(39) Meyer, R.; Broad, K.; Orlove, B.; Petrovic, N. Dynamic simulation as an approach to understanding hurricane risk response: Insights from the Stormview lab. *Risk Anal.* **2013**, *33*, 1532−1552.
(40) Li, Y.; Macdonald, D. D.; Yang, J.; Qiu, J.; Wang, S. Point defect model for the corrosion of steels in supercritical water: Part I, film growth kinetics. *Corros. Sci.* **2020**, *163*, 108280.
(41) Chapnevis, A.; Güvenç, I.; Bulut, E. Traffic Shifting based Resource Optimization in Aggregated IoT Communication. *2020 IEEE 45th Conference on Local Computer Networks (LCN)*; IEEE, 2020; pp 233−243.
(42) Kalantari, S. S.; Taleizadeh, A. A. Mathematical modelling for determining the replenishment policy for deteriorating items in an EPQ model with multiple shipments. *Int. J. Syst. Sci.: Oper. Logist.* **2020**, *7*, 164−171.
(43) Chapnevis, A.; Güvenç, İ.; Njilla, L.; Bulut, E. Collaborative Trajectory Optimization for Outage-aware Cellular-Enabled UAVs. *2021 IEEE 93rd Vehicular Technology Conference (VTC2021-Spring)*; IEEE, 2021; pp 1−6.
(44) Masoumnezhad, M.; Rajabi, M.; Chapnevis, A.; Dorofeev, A.; Shateyi, S.; Kargar, N. S.; Nik, H. S. An Approach for the Global Stability of Mathematical Model of an Infectious Disease. *Symmetry* **2020**, *12*, 1778.
(45) Arasteh, S.; Mahdavi, M.; Bideh, P. N.; Hosseini, S.; Chapnevis, A. Security Analysis of two Key Based Watermarking Schemes Based on QR Decomposition. *Electrical Engineering (ICEE), Iranian Conference on*; IEEE, 2018; pp 1499−1504.
(46) Chapnevis, A.; Sadeghiyan, B. A Secure Two-Party Computation Protocol for Intersection Detection between Two Convex Hulls, **2020**. arXiv:2011.00319.
(47) Peltonen, L.; Hirvonen, J.; Yliruusi, J. The effect of temperature on sorbitan surfactant monolayers. *J. Colloid Interface Sci.* **2001**, *239*, 134−138.
(48) Allen, W. J.; Lemkul, J. A.; Bevan, D. R. GridMAT-MD: a grid-based membrane analysis tool for use with molecular dynamics. *J. Comput. Chem.* **2009**, *30*, 1952−1958.
(49) Ritwiset, A.; Krongsuk, S.; Johns, J. R. Molecular structure and dynamical properties of niosome bilayers with and without cholesterol incorporation: A molecular dynamics simulation study. *Appl. Surf. Sci.* **2016**, *380*, 23−31.
(50) Akashi, K.; Miyata, H.; Itoh, H.; Kinosita, K., Jr. Preparation of giant liposomes in physiological conditions and their characterization under an optical microscope. *Biophys. J.* **1996**, *71*, 3242−3250.
(51) Danhier, F.; Feron, O.; Préat, V. To exploit the tumor microenvironment: passive and active tumor targeting of nanocarriers for anti-cancer drug delivery. *J. Controlled Release* **2010**, *148*, 135−146.
(52) Nguyen, T. T.; Shklovskii, B. I. Complexation of DNA with positive spheres: phase diagram of charge inversion and reentrant condensation. *J. Chem. Phys.* **2001**, *115*, 7298−7308.
(53) Bordi, F.; Cametti, C.; Diociaiuti, M.; Sennato, S. Large equilibrium clusters in low-density aqueous suspensions of poly-electrolyte-liposome complexes: a phenomenological model. *Phys. Rev. E* **2005**, *71*, 050401.
(54) Honary, S.; Ebrahimi, P.; Tabbakhian, M.; Zahir, F. Formulation and characterization of doxorubicin nanovesicles. *J. Vac. Sci. Technol., B: Microelectron. Nanometer Struct.–Process., Meas., Phenom.* **2009**, *27*, 1573−1577.
(55) Capoccia, E.; Cirillo, C.; Marchetto, A.; Tiberi, S.; Sawikr, Y.; Pesce, M.; D'Alessandro, A.; Scuderi, C.; Sarnelli, G.; Cuomo, R.; Steardo, L.; Esposito, G. S100B-p53 disengagement by pentamidine promotes apoptosis and inhibits cellular migration via aquaporin-4 and metalloproteinase-2 inhibition in C6 glioma cells. *Oncol. Lett.* **2015**, *9*, 2864−2870.
(56) Slee, E. A.; Adrain, C.; Martin, S. J. Executioner caspase-3,-6, and-7 perform distinct, non-redundant roles during the demolition phase of apoptosis. *J. Biol. Chem.* **2001**, *276*, 7320−7326.
(57) McIlwain, D. R.; Berger, T.; Mak, T. W. Caspase functions in cell death and disease. *Cold Spring Harbor Perspect. Biol.* **2015**, *7*, a026716.
(58) Arakawa, Y.; Saito, S.; Yamada, H.; Aiba, K. Simultaneous treatment with camptothecin and valproic acid suppresses induction of Bcl-X L and promotes apoptosis of MCF-7 breast cancer cells. *Apoptosis* **2009**, *14*, 1076−1085.
(59) Shi, C.; Zhang, X.; Zhang, X.; Chen, P.; Xu, L. Ultrasonic desulfurization of amphiphilic magnetic-Janus nanosheets in oil-water mixture system. *Ultrason. Sonochem.* **2021**, *76*, 105662.
(60) Singh, T.; Shukla, S.; Kumar, P.; Wahla, V.; Bajpai, V. K.; Rather, I. A. Application of nanotechnology in food science: perception and overview. *Front. Microbiol.* **2017**, *8*, 1501.
(61) Garbuzenko, O. B.; Mainelis, G.; Taratula, O.; Minko, T. Inhalation treatment of lung cancer: the influence of composition, size and shape of nanocarriers on their lung accumulation and retention. *Cancer Biol. Med.* **2014**, *11*, 44.
(62) Kafshdooz, L.; Kahroba, H.; Kafshdooz, T.; Roghayeh Sheervalilou, R.; Pourfathi, H. Labour analgesia; Molecular pathway and the role of nanocarriers: a systematic review. *Artif. Cells, Nanomed., Biotechnol.* **2019**, *47*, 927−932.
(63) Gil-Henn, H.; Destaing, O.; Sims, N. A.; Aoki, K.; Alles, N.; Neff, L.; Sanjay, A.; Bruzzaniti, A.; De Camilli, P.; Baron, R.; Schlessinger, J. Defective microtubule-dependent podosome organization in osteoclasts leads to increased bone density in Pyk2−/− mice. *J. Cell Biol.* **2007**, *178*, 1053−1064.
(64) Kamihara, Y.; Takada, K.; Sato, T.; Kawano, Y.; Murase, K.; Arihara, Y.; Kikuchi, S.; Hayasaka, N.; Usami, M.; Iyama, S.; Miyanishi, K.; Sato, Y.; Kobune, M.; Kato, J. The iron chelator deferasirox induces apoptosis by targeting oncogenic Pyk2/β-catenin signaling in human multiple myeloma. *Oncotarget* **2016**, *7*, 64330.
(65) Shapira, S.; Raanani, P.; Samara, A.; Nagler, A.; Lubin, I.; Arber, N.; Granot, G. Deferasirox selectively induces cell death in the clinically relevant population of leukemic CD34+ CD38−cells through iron chelation, induction of ROS, and inhibition of HIF1α expression. *Exp. Hematol.* **2019**, *70*, 55−69.
(66) Yang, X.-H.; Sladek, T. L.; Liu, X.; Butler, B. R.; Froelich, C. J.; Thor, A. D. Reconstitution of caspase 3 sensitizes MCF-7 breast cancer cells to doxorubicin-and etoposide-induced apoptosis. *Cancer Res.* **2001**, *61*, 348−354.
(67) Devarajan, E.; Sahin, A. A.; Chen, J. S.; Krishnamurthy, R. R.; Aggarwal, N.; Brun, A.-M.; Sapino, A.; Zhang, F.; Sharma, D.; Yang, X.-H.; Tora, A. D.; Mehta, K. Down-regulation of caspase 3 in breast cancer: a possible mechanism for chemoresistance. *Oncogene* **2002**, *21*, 8843−8851.
(68) Baharara, J.; Ramezani, T.; Divsalar, A.; Mousavi, M.; Seyedarabi, A. Induction of apoptosis by green synthesized gold nanoparticles through activation of caspase-3 and 9 in human cervical cancer cells. *Avicenna J. Med. Biotechnol.* **2016**, *8*, 75.

https://doi.org/10.1021/acsomega.1c03816
ACS Omega 2021, 6, 24218−24232

(69) Muzzalupo, R.; Tavano, L.; La Mesa, C. Alkyl glucopyranoside-based niosomes containing methotrexate for pharmaceutical applications: Evaluation of physico-chemical and biological properties. *Int. J. Pharm.* **2013**, *458*, 224−229.
(70) Sharma, V.; Anandhakumar, S.; Sasidharan, M. Self-degrading niosomes for encapsulation of hydrophilic and hydrophobic drugs: an efficient carrier for cancer multi-drug delivery. *Mater. Sci. Eng., C* **2015**, *56*, 393−400.
(71) Sah, A. K.; Vyas, A.; Suresh, P. K.; Gidwani, B. Application of nanocarrier-based drug delivery system in treatment of oral cancer. *Artif. Cells, Nanomed., Biotechnol.* **2018**, *46*, 650−657.
(72) Barani, M.; Mirzaei, M.; mahani, M. T.; Nematollahi, M. H. Lawsone-loaded Niosome and its Antitumor Activity in MCF-7 Breast Cancer Cell Line: A Nano-herbal Treatment for Cancer. *Daru, J. Fac. Pharm., Tehran Univ. Med. Sci.* **2018**, *26*, 11−17.
(73) Sommer, B.; Dingersen, T.; Gamroth, C.; Schneider, S. E.; Rubert, S.; Krüger, J.; Dietz, K.-J. CELLmicrocosmos 2.2 MembraneEditor: a modular interactive shape-based software approach to solve heterogeneous membrane packing problems. *J. Chem. Inf. Model.* **2011**, *51*, 1165−1182.
(74) Chen, F.; Smith, P. E. *Simulated Surface Tensions of Common Water Models*; American Institute of Physics, 2007.
(75) Malde, A. K.; Zuo, L.; Breeze, M.; Stroet, M.; Poger, D.; Nair, P. C.; Oostenbrink, C.; Mark, A. E. An automated force field topology builder (ATB) and repository: version 1.0. *J. Chem. Theory Comput.* **2011**, *7*, 4026−4037.
(76) van Gunsteren, W. F.; Berendsen, H. J. *Groningen Molecular Simulation (GROMOS) Library Manual*; Biomos: Groningen, 1987; Vol. *24*, p 682704, 13.
(77) Schmid, N.; Eichenberger, A. P.; Choutko, A.; Riniker, S.; Winger, M.; Mark, A. E.; van Gunsteren, W. F. Definition and testing of the GROMOS force-field versions 54A7 and 54B7. *Eur. Biophys. J.* **2011**, *40*, 843−856.
(78) Nasseri, B. Effect of cholesterol and temperature on the elastic properties of niosomal membranes. *Int. J. Pharm.* **2005**, *300*, 95−101.
(79) Berendsen, H. J. C.; Postma, J. P. M.; van Gunsteren, W. F.; DiNola, A.; Haak, J. R. Molecular dynamics with coupling to an external bath. *J. Chem. Phys.* **1984**, *81*, 3684−3690.
(80) Baranyai, A.; Evans, D. J. New algorithm for constrained molecular-dynamics simulation of liquid benzene and naphthalene. *Mol. Phys.* **1990**, *70*, 53−63.
(81) Berendsen, H. J. C.; van der Spoel, D.; van Drunen, R. GROMACS: a message-passing parallel molecular dynamics implementation. *Comput. Phys. Commun.* **1995**, *91*, 43−56.
(82) Petrović, S.; Tačić, A.; Savić, S.; Nikolić, V.; Nikolić, L.; Savić, S. Sulfanilamide in solution and liposome vesicles; in vitro release and UV-stability studies. *Saudi Pharm. J.* **2017**, *25*, 1194−1200.
(83) Mosmann, T. Rapid colorimetric assay for cellular growth and survival: application to proliferation and cytotoxicity assays. *J. Immunol. Methods* **1983**, *65*, 55−63.
(84) Mashayekhi, S.; Rasoulpoor, S.; Shabani, S.; Esmaeilizadeh, N.; Serati-Nouri, H.; Sheervalilou, R.; Pilehvar-Soltanahmadi, Y. Curcumin-loaded mesoporous silica nanoparticles/nanofiber composites for supporting long-term proliferation and stemness preservation of adipose-derived stem cells. *Int. J. Pharm.* **2020**, *587*, 119656.
(85) Karimi, A.; Sheervalilou, R.; Kahroba, H. A new insight on activation of human endogenous retroviruses (HERVs) in malignant melanoma upon exposure to CuSO4. *Biol. Trace Elem. Res.* **2019**, *191*, 70−74.

https://doi.org/10.1021/acsomega.1c03816
ACS Omega 2021, 6, 24218−24232